CO₂-assisted ethane aromatization over zinc and phosphorous modified ZSM-5 catalysts

Chunyan Tu [a,b,1], Huahua Fan [c,1], Dong Wang [a,1], Ning Rui [d], Yonghua Du [e], Sanjaya D. Senanayake [d], Zhenhua Xie [a,d,*], Xiaowa Nie [c,**], Jingguang G. Chen [a,d,*]

[a] Department of Chemical Engineering, Columbia University, New York, NY 10027, USA
[b] State Key Laboratory of Clean and Efficient Coal Utilization, Taiyuan University of Technology, Taiyuan 030024, China
[c] State Key Laboratory of Fine Chemicals, School of Chemical Engineering, Dalian University of Technology, Dalian 116024, China
[d] Chemistry Division, Brookhaven National Laboratory, Upton, NY 11973, USA
[e] National Synchrotron Light Source II, Brookhaven National Laboratory, Upton, NY 11973, USA

A B S T R A C T

The tandem reactions of CO₂-assisted oxidative dehydrogenation and aromatization (CO₂-ODA) of ethane were investigated over ZSM-5 modified with zinc (Zn) and phosphorus (P) by experimental studies and DFT calculations. The nature of active Zn species and their interaction with P were elucidated for understanding Zn/P-ZSM-5 catalyzed CO₂-ODA reaction of ethane. Compared to the direct dehydrogenation and aromatization (DDA) reaction, the Zn/P-ZSM-5 catalyst possessed higher ethane conversion, enhanced aromatics yield, and better stability in the CO₂-ODA reaction. The presence of CO₂ reduced the carbon deposition, stabilized the Zn species, and thereby facilitated the generation of more liquid aromatics in CO₂-assisted ethane aromatization. *In situ* characterization and DFT calculations provided insight into the mechanisms of CO₂-ODA over the Zn/P-ZSM-5 catalyst.

1. Introduction

Ethane is one of the main constituents of shale gas, while its dehydrogenated product, ethylene, is an important chemical raw material. Compared with the direct dehydrogenation of ethane, CO₂-oxidative dehydrogenation is a promising route to produce ethylene while converting CO₂, a main greenhouse gas, to CO. Previous studies have shown that the cleavage of the C–H bonds and C–C bonds of ethane can be tuned over a wide range of catalysts [1–5]. The tandem process of converting the ethylene product to value-added chemicals, such as aromatics [6], offers additional advantages in product separation. Traditionally, aromatics are obtained by catalytic cracking or naphtha reforming, which are energy-intensive and involve the consumption of crude oils. The selectivity toward aromatics has been studied on several metal-based catalysts for the direct dehydrogenation and aromatization (DDA) of ethane [7–10]. Ga/zeolite is a potential catalyst for the aromatics production from the DDA reaction, with the Ga species generating Lewis acid sites (LAS) for the aromatization reaction [11]. The

tandem reactions of CO₂ reduction and ethane aromatization provide a promising route for the synthesis of aromatics under ambient pressure. As reported earlier [12], Ga/ZSM-5 modified by phosphorus exhibited high activity toward aromatics from CO₂ and ethane with an aromatic yield of 13.7%.

Apart from Ga, Zn has been known to be able to convert ethane via the DDA reaction. The Zn²⁺ cation can interact with the Al sites on zeolite by charge compensation. Therefore, the addition of Zn to zeolite can induce a decrease of the Brønsted acid sites (BAS). The LAS provided by zinc could catalyze the initial light alkanes activation and subsequent oligomerization/aromatization [8,13], while BAS on acidic zeolite could promote the oligomerization of ethylene [14,15]. In addition, some transient BAS generated by C−H bond heterolysis of alkanes can accelerate the aromatization process [16]. However, ZnO in Zn/ZSM-5 can be reduced into metallic Zn under the conditions of ethane DDA reaction. The metallic Zn can evaporate from the catalyst bed, eventually leading to the Zn loss [17,18]. The zinc-based catalysts have shown problems of fast deactivation and low activity [19]. Therefore, it is

---

highly desirable to develop a stable Zn based catalyst with high activity.

Herein, Zn was loaded on the P-doped ZSM-5 zeolite, with a P loading of 0.4 wt%, and it was evaluated with ethane aromatization in the presence and absence of CO_2. The catalytic activity and kinetic studies over the Zn/0.4P-ZSM-5 catalyst provided information for the activation barriers and aromatics formation rate during the CO_2-assisted oxidative dehydrogenation and aromatization (CO_2-ODA). Ambient-pressure X-ray photoelectron spectroscopy (AP-XPS) and X-ray absorption fine structure (XAFS) techniques were used to characterize the structure of Zn/0.4P-ZSM-5 and active sites for the CO_2-ODA reaction of ethane. The presence of CO_2 was found to be able to stabilize the Zn/0.4P-ZSM-5 catalyst and enhance the aromatics yield. DFT calculations were also employed to further understand the active sites of the catalyst and the CO_2-ODA reaction mechanism.

2. Methods

2.1. Preparation of catalysts

NH4ZSM-5 zeolite with a SiO_2/Al_2O_3 molar ratio of 80 was purchased from Alfa Aesar. Before use, these ammonium-form ZSM-5 zeolites were calcined at 823 K for 4 h to obtain the proton-form ZSM-5 (H-ZSM-5) zeolites. Phosphoric acid (H_3PO_4, 85 wt% in H_2O), zinc nitrate ($Zn(NO_3)_2·6H_2O$) were purchased from Sigma Aldrich and used without further purification.

The P-ZSM-5 zeolites were prepared by impregnation of H-ZSM-5 with aqueous solution of phosphoric acid corresponding to 0.4 wt%. After impregnation, the resulting samples were dried at 373 K and finally calcined at 823 K in air for 4 h. Zn-modified ZSM-5 and P-ZSM-5 samples (containing 1.88 wt% Zn) were synthesized by slurry phase impregnation with zinc nitrate aqueous solution, followed by drying at 373 K and calcination at 823 K for 4 h, giving the samples Zn/ZSM-5 and Zn/0.4P-ZSM-5.

2.2. Catalytic evaluation

The catalytic performance of CO_2-assisted ethane aromatization was evaluated in a continuous-flow fixed-bed reactor at atmospheric pressure. Typically, the quartz tube with an inner diameter of 7 mm was loaded with 50 mg of catalyst (60–80 mesh). Prior to the reaction, the sample was pretreated *in situ* at 873 K for 1 h under Ar flow (10 mL/min). Then a mixture of 30 vol% ethane and 30 vol% CO_2 in Ar (10 mL/min total) was introduced into the reaction system and held at 873 K for 15 h. As for the DDA reaction of ethane, 30 vol% ethane in Ar (10 mL/min total) was used as the reactant gas. The reaction products were analyzed by an online Agilent 7890B gas chromatograph (GC) equipped with a thermal conductivity detector (TCD), a flame ionization detector (FID) and columns of two Haye Sep A, MolSieve 5 A and GS-GasPro. The molar flow rates of reactants and products were calculated by using Ar as the inner standard. Apparent activation energy and reaction order experiments were performed at higher space velocity and in turn lower conversion to apply the differential plug-flow reactor model.

2.3. Characterization of catalysts

Pyridine-adsorbed Fourier transform infrared spectroscopy (Py-FTIR) studies were conducted on the thermo scientific Nicolet 8700 spectrometer with an MCT detector. Before the measurement, the sample wafer was evacuated to 10^{-2} Pa at 623 K for 1 h. The adsorption of pyridine was performed at room temperature until equilibrium. Then the sample was heated to 623 K and evacuated for 30 min to remove physiosorbed pyridine. The Py-FTIR spectrum was recorded by collecting 32 scans at a resolution of 4 cm^{-1} in the transmission mode.

The ^{27}Al and ^{31}P solid-state magic-angle spinning nuclear magnetic resonance (MAS NMR) experiments were carried out on a Bruker Avance III 500 MHz spectrometer at resonance frequencies of 104.26 and

161.98 Hz, respectively, with a triple-resonance 5 mm probe. ^{27}Al MAS NMR spectra were recorded using a 0.4 μs π/12 excitation pulse with a recycling delay of 1 s. The ^{31}P MAS NMR spectra were recorded with a pulse width of 3 μs (ca. π/2 pulse) and a recycle delay of 30 s. Aluminum nitrate and ammonium phosphate were used as reference chemical compounds for ^{27}Al and ^{31}P MAS NMR, respectively. ^{29}Si MAS NMR measurements were conducted on a Bruker Avance III 600 MHz spectrometer with a sample spinning rate of 8 kHz using a 4-mm MAS probe with ZrO_2 rotor. ^{1}H MAS NMR spectra were collected using a Bruker 4 mm HX MAS NMR probe at the resonance frequency of 500.1 Hz, with a spinning rate of 10 kHz with a recycle delay of 5 s. Single-pulse excitation with a π/2 pulse length of 3.04 μs was used to acquire the data.

The carbonaceous deposit on the catalyst was studied by a Setaram thermogravimetric analyzer coupled with a mass spectrometer (TG-MS). The spent catalyst was heated up to 1073 K under air atmosphere (100 mL/min) with a ramp of 10 K/min. Meanwhile, CO_2 ($m/z = 44$) in the effluent was continuously recorded by MS. The Thermo iCAP 6300 inductively coupled plasma-atomic emission spectroscopy (ICP-AES) was used to measure the Zn and P contents in the fresh catalysts and spent catalysts after the reaction.

The AP-XPS experiments were performed on a commercial SPECS AP-XPS chamber equipped with a PHOIBOS 150 EP MCD-9 analyzer. Before the test, powder catalysts were pretreated in the fixed-bed reactor at 873 K for 1 h under Ar flow. Typically, the catalyst was pressed onto an aluminum plate and loaded into the AP-XPS chamber. The XPS spectra of the fresh sample were collected in vacuum at room temperature. Then, a mixture of 50 mTorr CO_2 and 50 mTorr ethane was introduced into the chamber. The spectra at the Zn 2*p*, Si 2*p*, Al 2*p*, C 1*s* and O 1*s* XPS regions were collected at 298 K and 800 K after 1 h treatment. The Si 2*p* was used for the binding energy calibration of the Zn 2*p*, Al 2*p*, C 1*s* and O 1*s* peaks.

The XAFS measurements were performed at beamlines 7-BM (QAS) and 8-BM (TES) of the National Synchrotron Light Source II (NSLS-II) in Brookhaven National Laboratory. The *in situ* Zn K-edge spectra were collected at beamline 7-BM for both the Zn/ZSM-5 and Zn/0.4P-ZSM-5 samples. For each *in situ* experiment, an appropriate amount of sample (60–80 mesh) was loaded into a home-made copper cell [3] and fixed by quartz wool on both sides. The cell windows were sealed with graphite carbon paper that is transparent for hard X-ray, allowing both transmission and fluorescence signals to be measured simultaneously. The sample was heated to 823 K within 30 min under He atmosphere (20 mL/min) and held for 30 min, after which it was exposed to the reaction mixture ($CO_2/C_2H_6/He = 5/5/10$ mL/min) at 823 K for 40 min. The P K-edge spectra were measured *ex situ* with a fluorescence mode at beamline 8-BM to investigate the local environment of P in the samples. Details about the analysis of XAFS results are provided in the SI.

2.4. DFT calculations

Periodic DFT calculations were performed using the Vienna *Ab-initio* Simulation Package (VASP) with the ion cores calculated by the projector augmented wave (PAW) pseudopotentials [20–22]. The exchange and correlation energies were treated using the generalized gradient approximation (GGA) with the Perdew−Burke−Ernzerh of (PBE) functional [23]. The PBE+D3 method was adopted to consider the dispersion interactions of the zeolite-containing system [24,25]. The cutoff energy of the plane-wave basis set was set to 400 eV and a Γ-point was applied for all calculations. Structure optimizations were considered to be converged when the forces on all atoms were less than 0.05 eV/Å. Transition states were searched using the climbing image nudged elastic band (CI-NEB) method [26]. Each transition state was ensured to have a single imaginary vibrational frequency along the reaction coordinate.

The MFI-type zeolite unit cell including 288 atoms was chosen as the computational model of ZSM-5 with an experimentally determined lattice constant of 20.02 Å × 19.90 Å × 13.38 Å. Based on the literature [13,27], two Si atoms located at the T8 and T12 sites within two

adjacent 5-membered rings of the straight channel were replaced by two Al atoms and the Brønsted acid sites of ZSM-5 were created by adding two H atoms bound to bridge O atoms of two -Si-O-Al- units to compensate the framework negative charge with Al substitution. Due to a better catalytic activity toward ethane transformation to benzene over Zn/ZSM-5 identified in the previous work [7], the [Zn-O-Zn]$^{2+}$ species was chosen as the main active site in this work, and thus the two protons (H$^+$) of HZSM-5 were exchanged by a Zn-O-Zn linker to construct the Zn/ZSM-5 model (Fig. S1A). The active site for catalyzing the reaction over Zn/P-ZSM-5 was considered as in the form of zinc phosphate-like active species (simplified as P-O-Zn), resulting from the transformation of weak Brønsted acid of H$_4$PO$_4$ and [Zn-O-Zn]$^{2+}$ (Figs. S1B and 6A), as discussed in detail in the section of DFT calculations. In the process of structural optimization, all atoms included in the computational model were fully relaxed.

3. Results and discussion

3.1. CO$_2$-ODA activity over Zn/0.4P-ZSM-5

Results for ethane and CO$_2$ conversion, product selectivity and yield (on an ethane basis) for Zn/ZSM-5 and Zn/0.4P-ZSM-5 in CO$_2$-ODA and DDA reactions are displayed in Fig. 1. Compared to Zn/ZSM-5, the conversions of ethane and CO$_2$ slightly decreased with the addition of 0.4 wt% P in the CO$_2$-ODA reaction of ethane (Fig. 1A and B). However, the incorporation of P significantly enhanced the selectivity to aromatics (Fig. 1C), resulting in an enhanced yield of liquid aromatics for the CO$_2$-ODA reaction of ethane (Fig. 1D).

The initial ethane conversion and aromatics selectivity for Zn/0.4P-ZSM-5 in the CO$_2$-ODA reaction were about 17.0% and 28.6%, respectively (Fig. 1A and C). A comparable ethane conversion (21.4%) and a much higher aromatics selectivity of 49.1% were obtained initially for the catalyst in the DDA reaction. However, the ethane conversion and aromatics selectivity in the DDA reaction decreased sharply with time on stream in comparison with those in CO$_2$-ODA. Same trends could also be observed on the Zn/ZSM-5 catalyst. The quick deactivation under DDA reaction conditions may be related to the partial evaporation of Zn species and carbon deposition on the catalysts. After 15 h of reaction over the Zn/0.4P-ZSM-5 catalyst, the ethane conversion in DDA reaction (4.9%) was significantly lower than that in the CO$_2$-ODA reaction (10.2%) (Fig. 1A). The ethane conversion, aromatics selectivity and aromatics yield for the Zn/0.4P-ZSM-5 catalyst in CO$_2$-ODA reaction were found to be more stable than those in the DDA reaction.

Fig. 1E and F showed the impact of CO$_2$ on the product selectivity and yield, respectively, at the pseudo-steady state. The presence of CO$_2$ decreased the ethylene selectivity and increased the selectivity to aromatics (benzene, toluene and xylenes) for both Zn/ZSM-5 and Zn/0.4P-ZSM-5 (Fig. 1E). In the absence of CO$_2$, the ethylene and aromatics yields for Zn/0.4P-ZSM-5 were about 4.6% and 0.5%, respectively. In comparison, the Zn/0.4P-ZSM-5 catalyst showed higher yields of ethylene (8.5%) and aromatics (1.3%) in the presence of CO$_2$, demonstrating the positive effect of CO$_2$ on ethane aromatization (Fig. 1F). Furthermore, the addition of 0.4 wt% P into Zn/ZSM-5 increased the aromatics yield both in the presence and absence of CO$_2$, resulting from the enhancement of aromatics selectivity by P incorporation.

The Zn contents in Zn/ZSM-5 and Zn/0.4P-ZSM-5 catalysts before and after reaction were measured by ICP-AES (Table 1). After the DDA reaction, the Zn content sharply decreased from 1.81% to 0.62% for Zn/ZSM-5 and from 1.83% to 0.49% for Zn/0.4P-ZSM-5, suggesting that most of Zn species were evaporated during the DDA reaction. This could be attributed to the reduction of Zn species to the metallic form of Zn, which was prone to evaporation at high temperatures [17,18]. In the presence of CO$_2$, the Zn content after the CO$_2$-ODA reaction was determined to be 1.44% for Zn/ZSM-5 and 1.58% for Zn/0.4P-ZSM-5, indicating that the Zn evaporation could be largely suppressed. The presence of CO$_2$ could significantly inhibit the formation of molecular H$_2$ in both

the dehydrogenation and aromatization processes of ethane, thus avoiding the formation of metallic Zn. Fig. S2 showed ^{29}Si MAS NMR spectra of Zn/0.4P-ZSM-5 before and after the CO$_2$-ODA reaction. No significant variation in the Si/Al$_{NMR}$ ratio could be seen for the Zn/0.4P-ZSM-5 catalyst after the reaction, indicating the stable zeolite structure in the CO$_2$-ODA reaction.

The extent of carbonaceous deposit over spent catalysts after the DDA and CO$_2$-ODA reaction was characterized by TG-MS (Fig. S3 and Table S1). As listed in Table S1, in the DDA reaction, the P addition could significantly decrease the carbon deposition with the mass loss of 12.1% for Zn/ZSM-5 and 6.8% for Zn/0.4P-ZSM-5. The carbon deposition could be further decreased to 5.7% for Zn/ZSM-5 and 4.6% for Zn/0.4P-ZSM-5 with the presence of CO$_2$ in the CO$_2$-ODA reaction. This indicated that the presence of CO$_2$ could promote the consumption of carbon by the reverse Boudouard reaction of CO$_2$ + C → 2CO, thus decreasing the carbonaceous deposit rate during the reaction process. Additionally, either for the DDA or CO$_2$-ODA reaction of ethane, the carbon content of spent Zn/0.4P-ZSM-5 was less than that of spent Zn/ZSM-5, indicating that incorporating P into Zn/ZSM-5 could also inhibit the carbon deposition.

To further identify the reason for the quick deactivation of Zn/0.4P-ZSM-5 in the DDA reaction of ethane, consecutive regeneration using air after the DDA reaction of ethane and subsequently performing activity tests were made, and the results were shown in Fig. S4. The ethane conversion and aromatics selectivity of Zn/0.4P-ZSM-5 decreased over 400 min of time on stream. However, the regeneration with air at 873 K led to the recovery of catalytic performance, indicating that the deactivation of the catalyst was partially ascribed to carbon deposition, and that this deactivation was reversible.

3.2. Kinetic studies over Zn/0.4P-ZSM-5

Kinetic measurements were conducted to further investigate the CO$_2$-ODA of ethane over the Zn/0.4P-ZSM-5 catalyst. Results for conversions and product selectivity at different temperatures were shown in Fig. S5. The apparent activation energies were calculated by measuring the rates of reactant consumption and product formation in the temperature range of 813–853 K over Zn/0.4P-ZSM-5. As shown in the Arrhenius-type plots in Fig. 2, the apparent activation barriers for ethane activation and aromatics production were 100 kJ·mol^{-1} and 117 kJ·mol^{-1}, respectively. The apparent activation barrier for C$_2$H$_4$ production, 93 kJ·mol^{-1}, was lower than the previously reported value (124 kJ·mol^{-1}) for the Ga/ZSM-5/P(0.8) catalyst [12], suggesting that the formation of C$_2$H$_4$ was not the rate-determining step of the CO$_2$-ODA of ethane. The apparent activation barrier for CO$_2$ conversion was measured as 118 kJ·mol^{-1}, which was much lower than the reported value of 163 kJ·mol^{-1} for CO$_2$ activation barrier over Ga/ZSM-5/P(0.8) in the CO$_2$-ODA of ethane [12].

Results of conversions and aromatics selectivity for the Zn/0.4P-ZSM-5 catalyst following the vol% of reactant CO$_2$ and ethane in the feed were displayed in Fig. S6. Fig. 3A showed the aromatics formation rate as a function of CO$_2$ vol% from 10 vol% to 50 vol% at a constant ethane vol% of 15 vol%, which decreased with the increase of CO$_2$ vol% and then gradually leveled off. Increasing the CO$_2$ vol% in the feed negatively affected the production of aromatics from ethane, implying that CO$_2$ adsorbates and ethane-derived surface intermediates were likely to occupy the same catalytic sites for dehydrogenation and/or aromatics formation. In contrast, as displayed in Fig. 3B, the aromatics formation rate increased linearly as the ethane vol% increased from 10 vol% to 40 vol% and then started to remain nearly constant. Above results suggested that ethane and CO$_2$ were probably activated on one type of active sites on Zn/0.4P-ZSM-5 and the competitive adsorption of CO$_2$ impeded ethane adsorption and conversion.
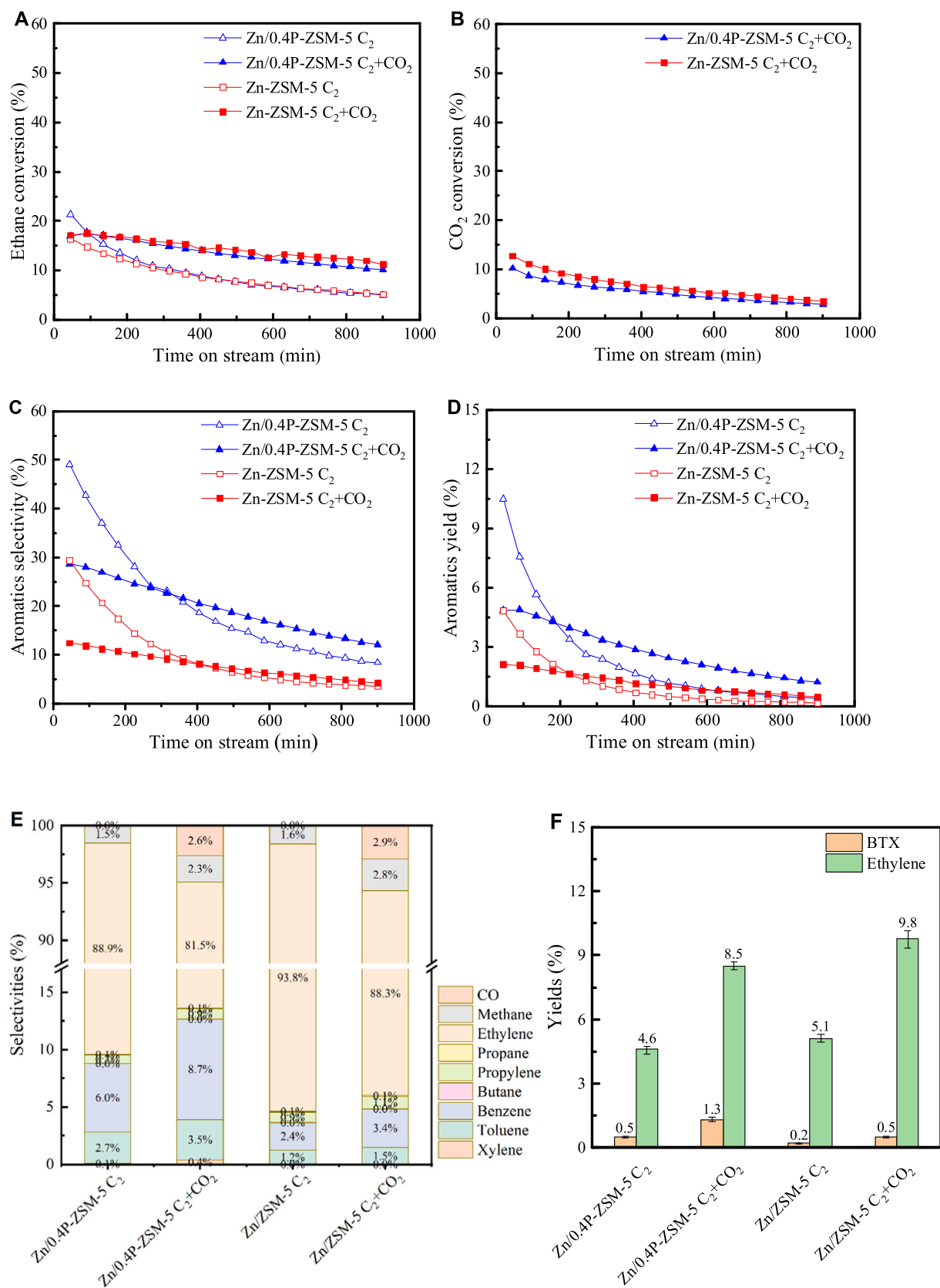
Fig. 1. Comparisons of catalytic performance of Zn/ZSM-5 and Zn/0.4P-ZSM-5 in CO_2-ODA and DDA reactions of ethane. Results of time on stream for (A) ethane conversion, (B) CO_2 conversion, (C) aromatics selectivity and (D) aromatics yield. The impact of CO_2 on (E) product selectivity and (F) the yields of aromatics and ethylene at the pseudo-steady state (values are obtained at the 800–900 min on stream). Reaction conditions: 873 K, $Ar/C_2H_6/CO_2 = 4/3/3$ mL/min or $Ar/C_2H_6 = 7/3$ mL/min, 50 mg of catalyst. Selectivity and yield are determined on a C_2H_6 basis.

Table 1
ICP-AES results of fresh catalysts and spent catalysts after reaction.

Sample	Reaction system	P content /wt%	Zn content /wt%
fresh Zn-ZSM-5	-	-	1.81
spent Zn-ZSM-5	C_2	-	0.62
	CO_2+C_2	-	1.44
fresh Zn/0.4P-ZSM-5	-	0.45	1.83
spent Zn/0.4P-ZSM-5	C_2	0.37	0.49
	CO_2+C_2	0.44	1.58

3.3. Ex situ and in situ characterization of catalysts

The coordination environments of Al and P species in the samples were studied by ^{27}Al MAS NMR and ^{31}P MAS NMR spectroscopy (Figs. S7 and 4A). As shown in Fig. S7, the ^{27}Al MAS NMR spectra of ZSM-5, Zn/ZSM-5, 0.4P-ZSM-5 and Zn/0.4P-ZSM-5 catalysts displayed a peak at around 55.0 ppm, corresponding to tetrahedrally coordinated Al atoms in the zeolite framework. A broader peak at about 39.0 ppm was observed for 0.4P-ZSM-5 and Zn/0.4P-ZSM-5, due to the presence of the distorted tetrahedrally coordinated Al atoms, although the occurrence of penta-coordinated Al atoms cannot be excluded [28]. The 0.4P-ZSM-5 catalyst also showed two signals of octahedral (extra framework lattice) Al at −10.0 and − 19.3 ppm. Fig. 4A compared the ^{31}P MAS NMR spectra for the 0.4P-ZSM-5 and Zn/0.4P-ZSM-5 catalysts. The

0.4P-ZSM-5 sample showed mainly three peaks at −13.1, −32.1 and −39.2 ppm; no monomeric phosphoric acid at 0 ppm was found for the two samples [29]. The peak at −13.1 ppm was assigned to the intermediate groups in short-chain polyphosphates or pyrophosphates [30], the peak at −32.1 ppm was due to the presence of aluminum phosphate [31], and the peak at − 39.2 ppm was attributed to highly condensed polyphosphate or polyphosphoric species. Peaks at − 32.1 and −39.2 ppm could also be assigned to $(SiO)_xAl(OP)_{4−x}$ species generated by the substitution of framework Si atoms by P[32]. Unlike 0.4P-ZSM-5, a sharp peak at 3.8 ppm was observed in the Zn/0.4P-ZSM-5 catalyst, which likely belonged to the unprotonated phosphate group connected to Zn cations [33]. The ^{1}H MAS NMR spectra of Zn/ZSM-5 and Zn/0.4P-ZSM-5 (Fig. 4B) showed two dominated peaks at 4.1 and 1.2 ppm, which were ascribed to the Si-OH-Al (Brønsted acid sites) and Zn-OH groups (hydroxylated Zn species), respectively [34,35]. The signal at 6.2 ppm was assigned to water molecules adsorbed on the Lewis acid sites. Combining the information from the ^{31}P MAS NMR and ^{1}H MAS NMR spectra, two types of Zn species were present on the Zn/0.4P-ZSM-5 catalyst, zinc phosphate-like species and Zn-OH species. Compared with Zn/ZSM-5, the amount of Zn-OH in the Zn/0.4P-ZSM-5 catalyst slightly decreased owing to the formation of zinc phosphate-like species. As shown by the IR spectra following pyridine adsorption (Fig. 4C), mainly BAS sites were observed in ZSM-5. Incorporating Zn into the ZSM-5 zeolite decreased the BAS sites and significantly increased the LAS sites. Compared to Zn/ZSM-5, a small amount of P
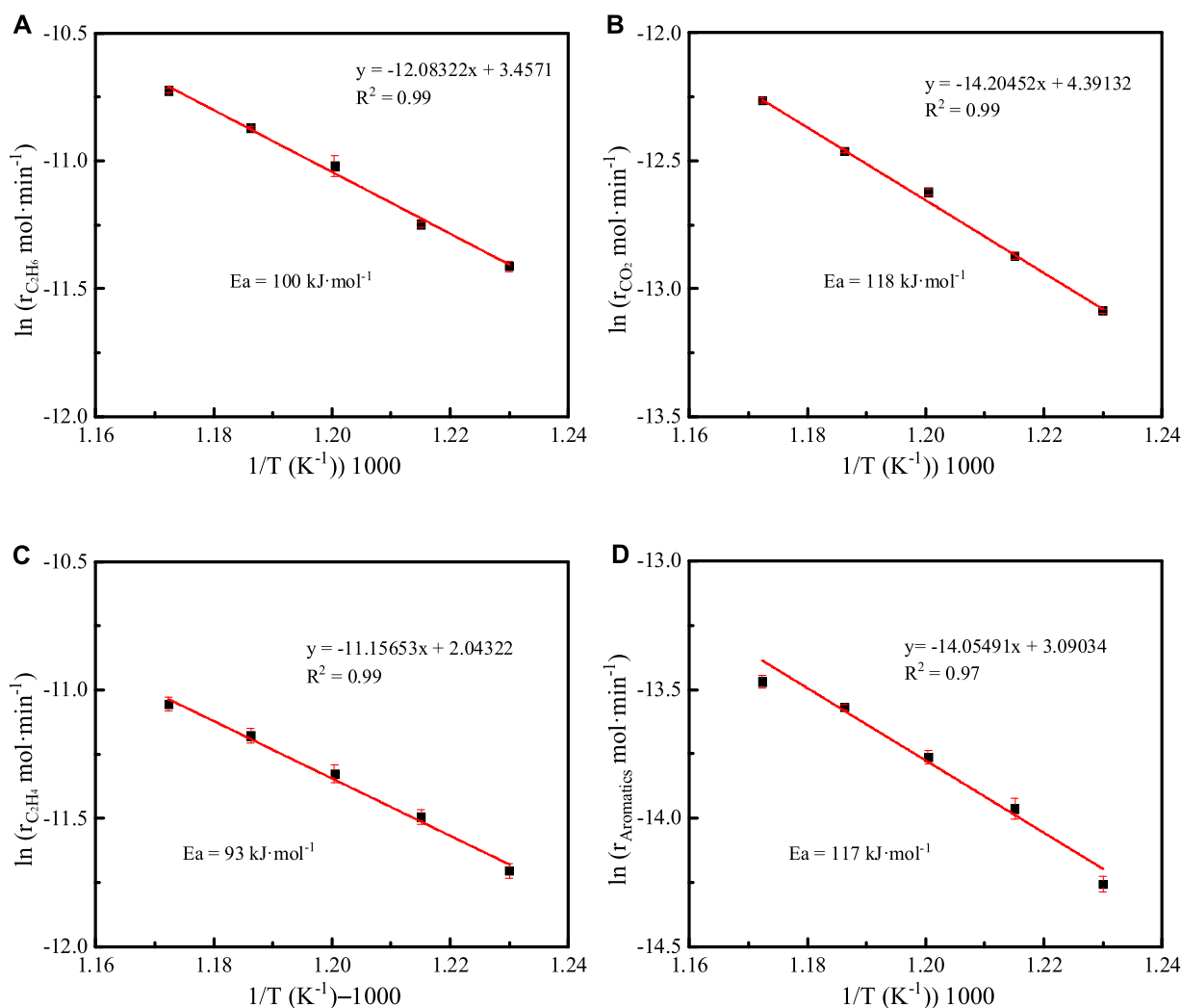

Fig. 2. Apparent activation energies obtained by varying temperature over a diluted Zn/0.4P-ZSM-5 catalyst for (A) C_2H_6 activation, (B) CO_2 activation, (C) C_2H_4 formation and (D) aromatics formation. Reaction conditions: 813–853 K, atmospheric pressure, a total flow rate of 20 mL·min^{-1} (C_2H_6: CO_2: Ar = 3: 3: 14).
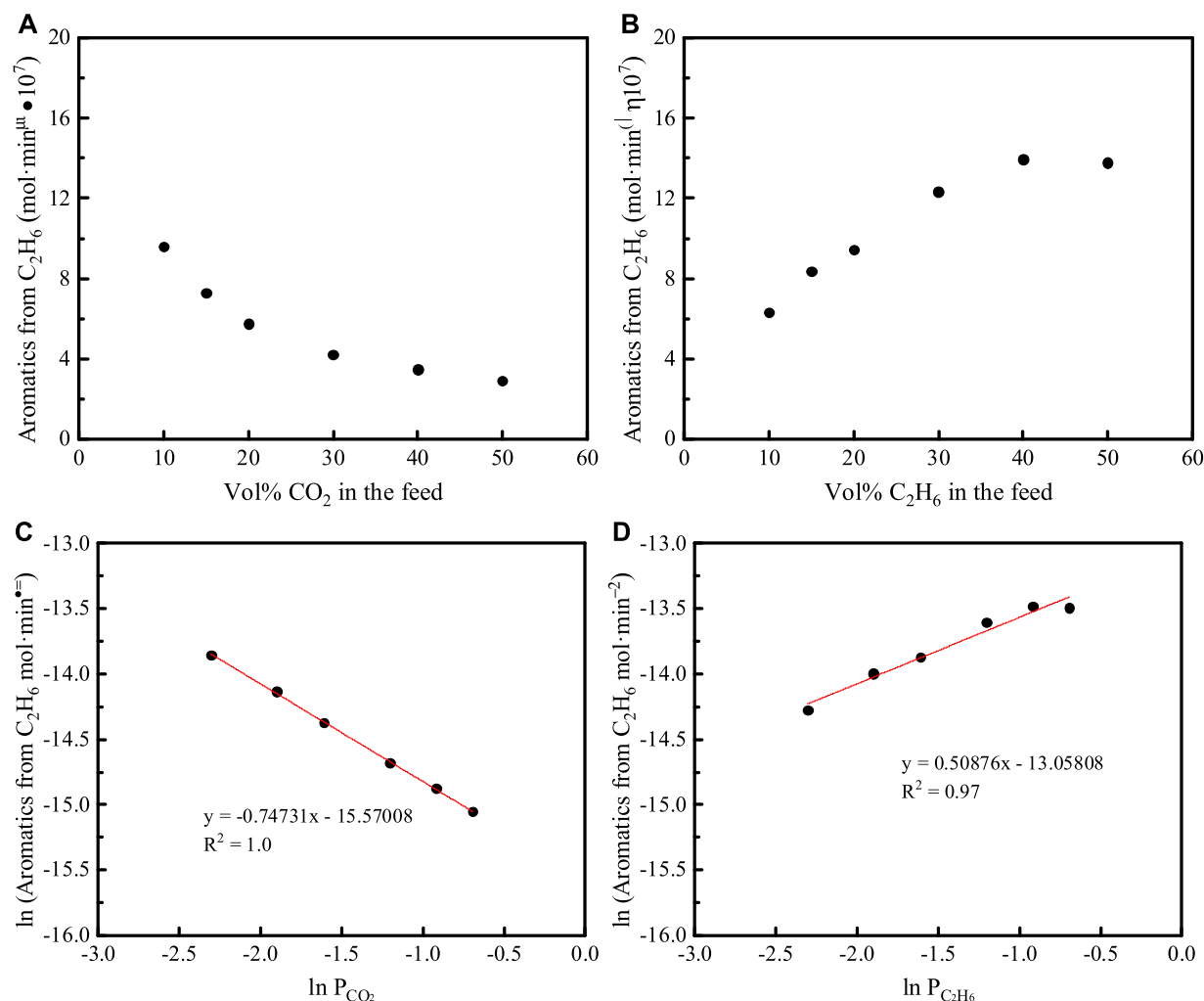
Fig. 3. Effect of the vol% of reactant CO_2(A) and C_2H_6 (B) in the feed on the formation rate of aromatics over a diluted Zn/0.4P-ZSM-5 catalyst. (C) Formation rate of aromatics versus CO_2 partial pressure. (D) Formation rate of aromatics versus C_2H_6 partial pressure. Reaction conditions: 843 K, atmospheric pressure, a total flow rate of 20 mL·min^{-1}, increasing one reactant content (10–50 vol%) while maintaining the other constant (15 vol%) by varying the Ar diluent accordingly.

(0.17 wt%) could both increase the BAS and LAS sites (Fig. S8 and Table S2). Further increasing the P content could decrease the LAS continuously, likely due to the formation of zinc phosphate-like species reducing the amount of Zn-OH species, while a decrease in BAS could result from the breaking of Si–OH–Al bonds in zeolite framework at high P concentration [36]. The influence of P modification on zeolites has been studied for methanol to hydrocarbons (MTH) reactions [36–39]. The presence of P was believed to change the shape selectivity of zeolites as well as the surface acidity [36,37,39,40]. It was found that the phosphorus species connected to local zeolite interfaces were related to the selectivity change in the MTH reaction [39], and the aromatic-based hydrocarbon pool mechanism was suppressed in this reaction by P modification [36]. In the current study, compared to Zn/ZSM-5, the Zn/0.4P-ZSM-5 catalyst had comparable amounts of BAS and LAS (Fig. S8 and Table S2). However, the Zn/0.4P-ZSM-5 catalyst showed a much higher selectivity to aromatics in both DDA and CO_2-ODA reaction of ethane. Notably, the LAS produced by Zn incorporation was demonstrated to catalyze the oligomerization/aromatization of olefinic intermediates in both ethane and isobutane aromatization reactions [8, 13], although BAS on acidic zeolite could oligomerize ethylene [14,15]. Therefore, the enhanced aromatics selectivity of Zn/0.4P-ZSM-5 by the P incorporation may be attributed to the generation of zinc phosphate-like species, as suggested by DFT calculations.

To further probe the local environment of P, *ex situ* XANES features at

the P K-edge were also measured. As shown in Fig. 4D, compared with the $Zn_3(PO_4)_2$ standard, both the spent 0.4P-ZSM-5 and Zn/0.4P-ZSM-5 samples demonstrated a more intense white line, suggesting a lower occupancy in the 3p states of P. Given the sensitivity of the intensity of white line and corresponding peak position to local geometry [41,42], a stronger white line centered at higher energy for 0.4P-ZSM-5 and Zn/0.4P-ZSM-5 indicated that P was most likely coordinated in a more symmetric environment than $Zn_3(PO_4)_2$ due to the substrate effect from ZSM-5, as described in Table S3.

In situ characterization was performed for the Zn/ZSM-5 and Zn/0.4P-ZSM-5 catalysts under reaction conditions. As shown in Fig. 5A, AP-XPS results revealed two types of Zn^{2+} species in ZSM-5 zeolite, including mononuclear Zn^{2+} and dinuclear $[ZnOZn]^{2+}$ cations derived from the dehydration of $[Zn(OH)]^+$ species [18,43,44]. The peak appeared at 1022.7 eV could be reasonably attributed to isolated $[Zn(OH)]^+$ and the peak at a higher binding energy value of 1024.1 eV could be assigned to isolated Zn^{2+} attributed to stronger binding of Zn^{2+} species to the framework oxygen of the zeolite [45,46]. The ZnO species at 1021.0–1021.8 eV was also observed for both samples at room temperature in the absence of the reaction gas. At room temperature, mainly $[Zn(OH)]^+$ existed in Zn/ZSM-5 and Zn/0.4P-ZSM-5 samples corresponding to the decrease of the Brønsted acid sites. The reaction conditions had significant influence on the type of the surface zinc species. The peak at 1022.7 eV shifted to higher binding energy (1024.1 eV),
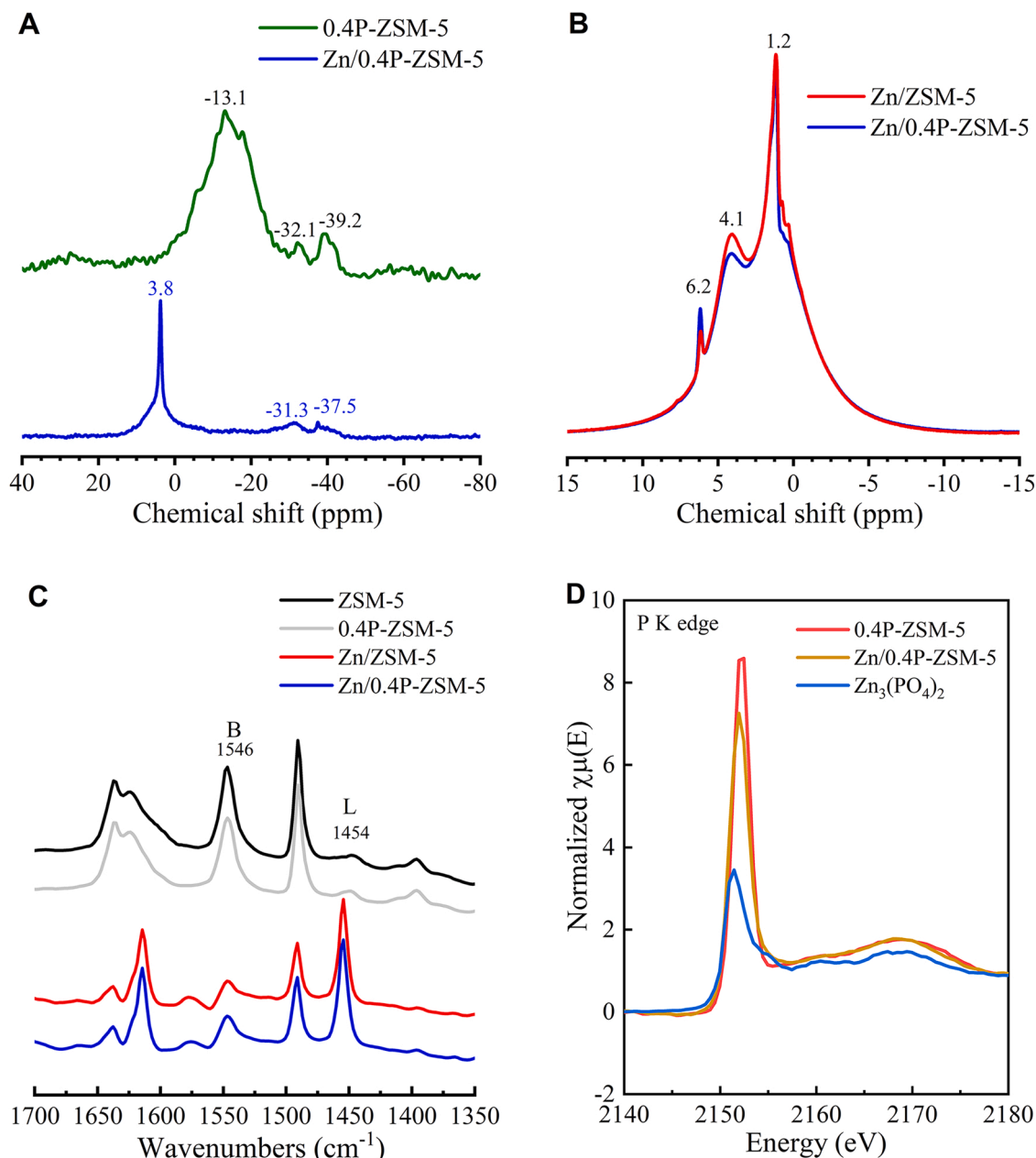
Fig. 4. (A) ^{31}P MAS NMR spectra of 0.4P-ZSM-5 and Zn/0.4P-ZSM-5 catalysts. (B) ^{1}H MAS NMR spectra of Zn/ZSM-5 and Zn/0.4P-ZSM-5 catalysts. (C) FTIR spectra of pyridine adsorption on ZSM-5, 0.4P-ZSM-5, Zn/ZSM-5 and Zn/0.4P-ZSM-5 catalysts. (D) *Ex situ* XANES features of P K-edge over the spent 0.4P-ZSM-5 and Zn/0.4P-ZSM-5 samples as well as the $Zn_3(PO_4)_2$ reference.

indicating the dehydration of $[Zn(OH)]^+$ species and the formation of isolated Zn^{2+} species in the presence of reactant gas at 800 K.

The *in situ* XAFS measurements were carried out at the Zn K-edge to explore the chemical states and local environment of Zn in the zeolite catalysts. As shown in Fig. 5B, both fresh Zn/ZSM-5 and Zn/0.4P-ZSM-5 samples exhibited strong white line peaks, indicating an oxidized state of Zn. It is noted that the edge position (9964.2 eV) and white line intensity were noticeably higher than the counterparts of ZnO (9661.4 eV) and Zn foil (9659.0 eV), consistent with the formation of pseudo-octahedral $[Zn(H_2O)_n]^{2+}$ or $[Zn(H_2O)_{n-1}(OH)]^+$ complexes (n = 6 or 5) due to the hydration of Zn cations by the atmospheric water [18,47]. This phenomenon was also in agreement with the AP-XPS analysis that hydrated Zn species dominated over the fresh sample. The EXAFS fitting results (see Table S4 in SI and Fig. 5C) of the Zn K-edge indeed showed a larger coordination number (CN) of the Zn-O bond [i.e., Zn/ZSM-5—5.4 and Zn/0.4P-ZSM-5—5.1] than that (4.0) of the typical hexagonal ZnO.

After pretreatment under the He atmosphere and then exposure to the reaction stream at 823 K, the Zn edge position shifted to lower energy (9662.9 eV for Zn/ZSM-5 and 9663.2 eV for Zn/0.4P-ZSM-5), but still higher than that of Zn foil and ZnO. Such observation was typical for Zn cations incorporated into the framework of ZSM-5 [47,48]. In addition, the strong white line diminished owing to the dehydration process with the appearance of two split peaks that were indicative of tetrahedral or square-pyramidal Zn complexes [48–50]. Correspondingly, the CN of the total number of Zn-O bonds (sum of Zn-O^a and Zn-O^b) over Zn/ZSM-5 was reduced to 4.0 under the reaction condition. It should be noted that the peak in the first nearest shell was broadly distributed, suggesting the existence of multiple Zn-O bonds with different bond lengths. Guided by the input from a DFT-optimized geometry (see Fig. S1A in SI), at least two types of Zn-O bond could be identified, i.e., a shorter Zn-O^a bond [CN: 3.3] at 1.95 Å and a longer Zn-O^b bond [CN: 0.7] at 2.44 Å. The large Debye-Waller factors (σ^2), 0.012 Å^2 for Zn-O^a
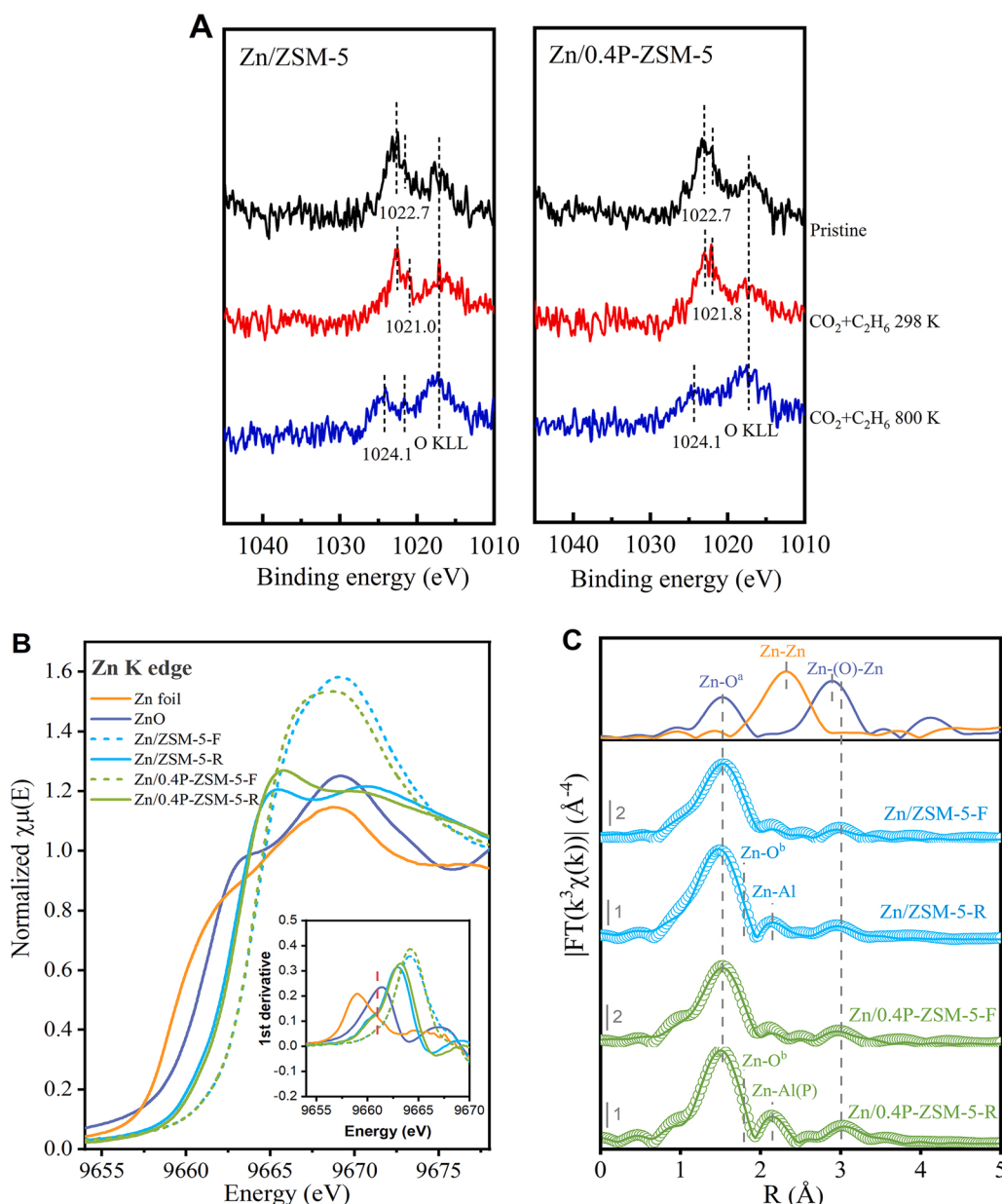
Fig. 5. *In situ* structural characterizations of Zn/ZSM-5 and Zn/0.4P-ZSM-5 catalysts. (A) AP-XPS spectra of Zn 2p of Zn/ZSM-5 and Zn/0.4P-ZSM-5 catalysts. (B) *In situ* XANES features of Zn K-edge over Zn/ZSM-5 and Zn/0.4P-ZSM-5 under fresh condition, He pretreatment at 823 K and reaction condition at 823 K as well as over standards (Zn foil and ZnO); the inset illustrates the first derivative of the normalized XANES curves. (C) *In situ* Fourier-transformed EXAFS signals in R space and fitting results of Zn K-edge for Zn/ZSM-5 and Zn/0.4P-ZSM-5; EXAFS plots of standards were also illustrated for comparison. Notes: Zn-O^a and Zn-O^b refer to the nearest and second nearest Zn-O bonds, respectively. The suffixes after sample names, "F" and "R", represent the sample under fresh and reaction conditions, respectively.

and 0.014 Å^2 for Zn-O^b, further suggested a high distortion of the four-coordinated environment of Zn even though the high measuring temperature may also contribute to a thermal disordering to some extents. A Zn-Al bond was observed at 2.63 Å with a CN of 0.7, which was in agreement with the incorporation of Zn cations in the zeolite framework (see Fig. S1A in SI), at which the shorter and longer Zn-O bonds in the nearest shell shared the same coordination center with the Zn-Al bond. In addition, minor ZnO-like species were observed, as indicated by the Zn-Zn bond [3.36(2) Å, CN of 1.0(3)] and the small shoulder (indicated by the red dashed line in the inset of Fig. 5B) at the similar position with that of ZnO in the first derivative of the XANES curves. This also coincided with the small signal of ZnO-like species from AP-XPS measurements. Thus, the model with isolated Zn cations incorporated in the ZSM-5 framework was adopted to depict the Zn/ZSM-5 catalyst. As indicated in the precious reports [18,51], the EXAFS results could not differentiate between the mono [O$^-$-Zn^{2+}-O$^-$] and dinuclear [Zn-O-Zn]$^{2+}$ type of isolated Zn cations since the scattering from the Zn-O-Zn bond in [Zn-O-Zn]$^{2+}$ was too weak to be extracted by EXAFS analysis. In the present work, the [Zn-O-Zn]$^{2+}$ type

was adopted as the dominant site given its better catalytic activity toward ethane transformation[7].

The observation of similar XAFS features over Zn/0.4P-ZSM-5 also indicated the dominance of framework Zn cations and the existence of minor ZnO-like species under the reaction condition. However, the slightly different XANES spectra over Zn/0.4P-ZSM-5 indicated a subtle difference in the local structure of Zn in the presence of P. The EXAFS fitting results indicated an average CN of ~3.3 for the total number of Zn-O bonds in the nearest shell, lower than that of the four-coordinated Zn cations in either zeolite framework or ZnO. This was most likely due to the interaction of Zn with the phosphate groups as suggested by the aforementioned ^{31}P NMR and P XANES analysis, based on which an initial DFT configuration with a zinc phosphate-like species was optimized (see Fig. S1B in SI). The model (Fig. 6A) presented a rather long Zn-O bond at ~2.7 Å, which would exhibit a weak or negligible backscattering feature under the high-temperature reaction condition and in turn hardly be extracted from the EXAFS analysis. Moreover, the similar CN (~0.5) of Zn-O^b with Zn-Al(P), implying the same coordination center, also agreed with the DFT model in Fig. 6A. It should be
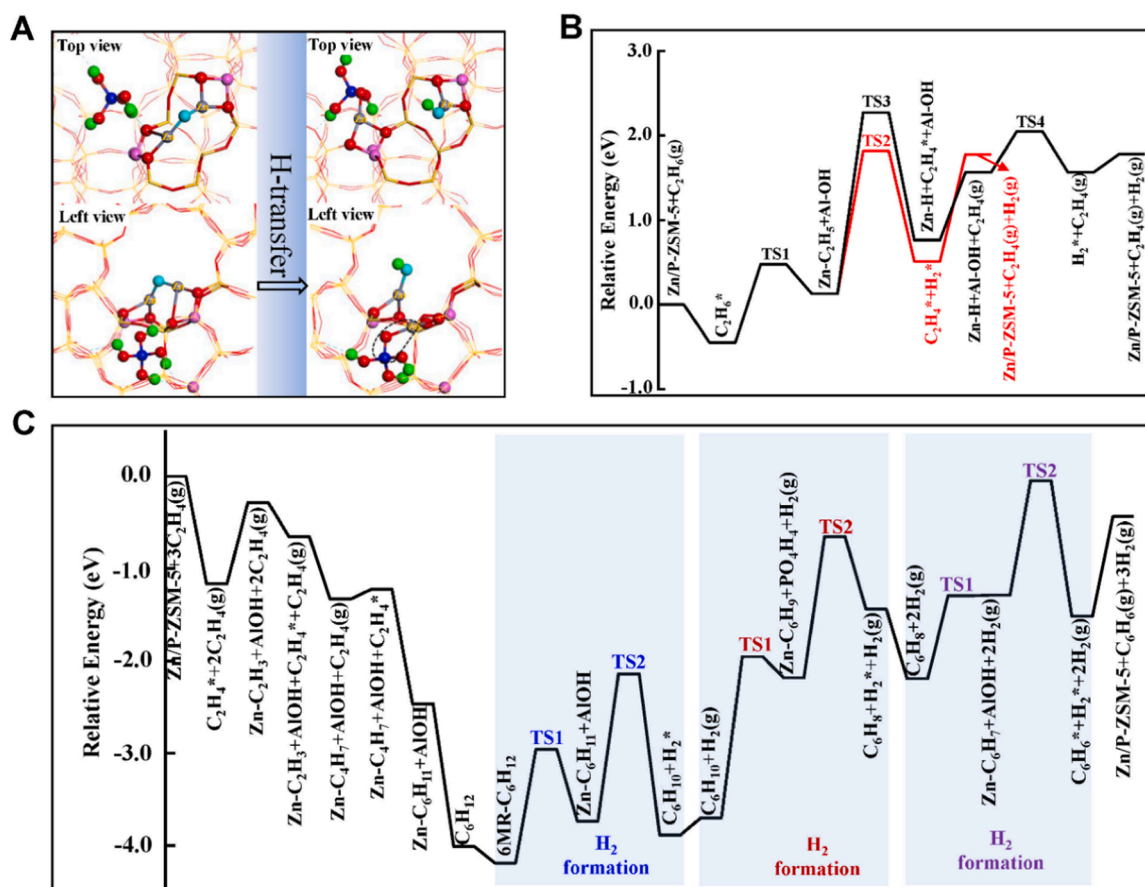
Fig. 6. The transformation of active site and energy diagrams of ethane aromatization over Zn/P-ZSM-5. (A) The transformation of weak Brønsted acid of H_4PO_4 and $[Zn-O-Zn]^{2+}$ to the new active site (simplified as P-O-Zn) of Zn/P-ZSM-5. (B) Ethane dehydrogenation to ethylene in the absence of CO_2. (C) Ethylene aromatization to benzene in the absence of CO_2 (Activation barriers of the three groups of H_2 generation steps are included.) (pink: Al, red: O, light purple: Zn, bright blue: O of [Zn-O-Zn]$^{2+}$, green: H of H_4PO_4, dark blue: P of H_4PO_4). (For interpretation of the references to color in this figure legend, the reader is referred to the web version of this article.)

noted that the bond at 2.64(3) Å was assigned to Zn-Al and/or Zn-P because they exhibited a similar and indistinguishable scattering feature (see the Feff calculations in Fig. S9 in SI).

3.4. DFT results

3.4.1. The DDA mechanism over Zn/P-ZSM-5 catalyst

To gain insight into the mechanism of ethane conversion from the molecular level, DFT calculations were performed for ethane DDA over Zn/P-ZSM-5. With P modification of ZSM-5, the H_4PO_4 species was easy to form near the framework Al via interacting with the proton of Brønsted acid [28]. Upon the introduction of P into Zn/ZSM-5, a Zn atom of $[Zn-O-Zn]^{2+}$ replaced a H atom of H_4PO_4 to form a Zn-OH and a new zinc phosphate-like active species (See Figs. S1B and 6A) in which the coordination of Zn with surrounding O was consistent with the EXAFS analysis. Focusing on the role of the new zinc phosphate active species (simplified as P-O-Zn species, as shown in the black dashed circle of Fig. 6A) in ethane conversion, DFT results provided insight into the interaction between P and Zn. After the adsorption of ethane over the new P-O-Zn site, the C-H bond was activated and cleaved, forming either the (Zn-C_2H_5 and -OH) or (Zn-H and O-C_2H_5) species. The energy barriers for the two pathways were calculated to be 0.93 and 2.88 eV, respectively, indicating that the formation of the Zn-C_2H_5 intermediate was kinetically more favorable in initial ethane conversion. Subsequently, the β-H abstraction of Zn-C_2H_5 went through two different paths, either forming ethylene+Zn-H via H transfer to Zn or directly forming ethylene+H_2 via H transfer to -OH. The barriers of these two

paths were calculated to be 2.14 and 1.69 eV, respectively. Thus, the latter path was kinetically favored, with the H of C_2H_5 transferred to -OH combined with the regeneration of the P-O-Zn active site. The energy diagram of ethane dehydrogenation over the P-O-Zn site based on electronic energy calculation at 0 K was shown in Fig. 6B, and the Gibbs free energy diagram calculated at the reaction temperature of 873 K was provided in Fig. S10A. The corresponding structures for all elementary steps involved were provided in Fig. S11. As demonstrated in Fig. 6B, the β-H abstraction of Zn-C_2H_5 was the rate-limiting step in ethane dehydrogenation to ethylene over Zn/P-ZSM-5, which had a barrier of 1.69 eV (shown as the red line in Fig. 6B). Compared to the rate-limiting barrier of 1.83 eV in ethane dehydrogenation over Zn/ZSM-5 in a previous study [7], the interaction between P and Zn in the new zinc phosphate active species over Zn/P-ZSM-5 positively impacted the conversion of ethane, as observed experimentally in Fig. 1.

As shown in Fig. 1E, benzene was the major product in aromatics production experimentally. Therefore, DFT calculations of benzene formation were performed to further examine the pathways and energetics of ethylene aromatization to aromatics over Zn/P-ZSM-5. The energy diagram based on electronic energy calculation at 0 K was plotted in Fig. 6C and the Gibbs free energy diagram calculated at the reaction temperature of 873 K was provided in Fig. S10B. The optimized reactant, intermediate and product structures were provided in Fig. S12. After the adsorption of ethylene on the P-O-Zn site, benzene was generated via consecutive steps of oligomerization, cyclization, and the formation and desorption of H_2. In previous studies [7,12,52], it was considered that the generation of H_2 was difficult and limiting the rate

for aromatics production. As demonstrated in the reaction energy diagram in Fig. 6C, the three groups of dehydrogenation reactions were endothermic, thus barrier calculations were further performed for these steps. The activation barriers associated with the three groups of H_2 generation reactions were (1.23 eV_TS1, 1.60 eV_TS2), (1.74 eV_TS1, 1.53 eV_TS2), and (0.90 eV_TS1, 1.24 eV_TS2), as shown in Fig. 6C. The barrier of the rate-limiting step (1.74 eV) for ethylene aromatization to benzene over Zn/P-ZSM-5 was 0.1 eV lower than that (1.84 eV) obtained over Zn/ZSM-5 in a previous study [7], indicating that the modification of P had a positive effect toward aromatics production. Based on the energy diagrams shown in Fig. 6, it was revealed that benzene formation proceeded more slowly than ethylene production over Zn/P-ZSM-5 by comparing either the rate-limiting barriers (1.74 vs. 1.69 eV) or effective barriers (4.14 vs. 2.27 eV) of the overall reaction, which is consistent with the experimental kinetic studies. The effective barrier dictates the energy difference between the lowest energy state and the highest transition state in the energy diagrams as shown in Figs. 6B and 6C for the two reactions.

3.4.2. The effect of CO_2 on reaction performance

The experimental results in Fig. 1 showed that, in the presence of CO_2, ethane conversion and aromatic selectivity over Zn/P-ZSM-5 were lower than those without CO_2 at the beginning of the reaction. However, as the reaction time increased, the presence of CO_2 promoted ethane conversion while the selectivity to aromatics gradually exceeded that without CO_2. Based on the results of TG-MS and ICP-AES, it indicated that CO_2 had a positive influence on inhibiting Zn loss, reducing carbon deposition and improving catalyst stability. Therefore, the impact of CO_2 on ethane aromatization over Zn/P-ZSM-5 was further studied in

this work. The co-feeding of CO_2 may inhibit the loss of metallic Zn and increase the catalyst stability through hydrogen consumption and the reverse Boudouard reaction. Therefore, DFT calculations were conducted to study the intrinsic effect of CO_2.

In the literature, the reactions between CO_2 and the metal-H precursor involved in the H_2 generation step were reported [12,52,53]. In the conversion of ethane to ethylene involving CO_2, the Zn-H species reacted with CO_2 to generate a Zn-OC(H)O intermediate instead of reacting with -OH to generate H_2 in the absence of CO_2, leading to an increased barrier from 0.49 to 0.95 eV (see the Fig. 7A). The formed Zn-OC(H)O species was more likely to react with -OH to generate Zn-HCOOH, which was an exothermic reaction and had no barrier (see the Fig. 7A), instead of forming H_2O and CO that had a large barrier of 2.94 eV. Relevant structures were provided in Fig. 7A. Although the barrier of CO_2 reacting with Zn-H increased, CO_2 co-feeding had no influence on the rate-limiting step of ethane dehydrogenation to ethylene, which was still the β-H transfer of Zn-C_2H_5 to regenerate the Zn site with a barrier 2.14 eV (black line shown in Fig. 6B). These results indicated that CO_2 did not promote ethane conversion to ethylene but could circumvent the generation of H_2. The decrease of H_2 concentration could inhibit the reduction and consequently the evaporation of metallic Zn [54]. The path of reaction between Zn-H and CO_2 over Zn-based SSZ-13 catalysts in the literature [53] was similar to that over Zn/P-ZSM-5 in this work. In addition, the adsorption of CO_2 and ethane over the Zn-OH site and the -OH of PO_4H_4 (denoted as P-OH site) was also studied and compared with their adsorption over the P-O-Zn site. The adsorption energy diagram and all possible adsorption structures are provided in Figs. S13 and S14. It can be seen that among the three types of adsorption sites, the P-O-Zn site has a stronger binding ability
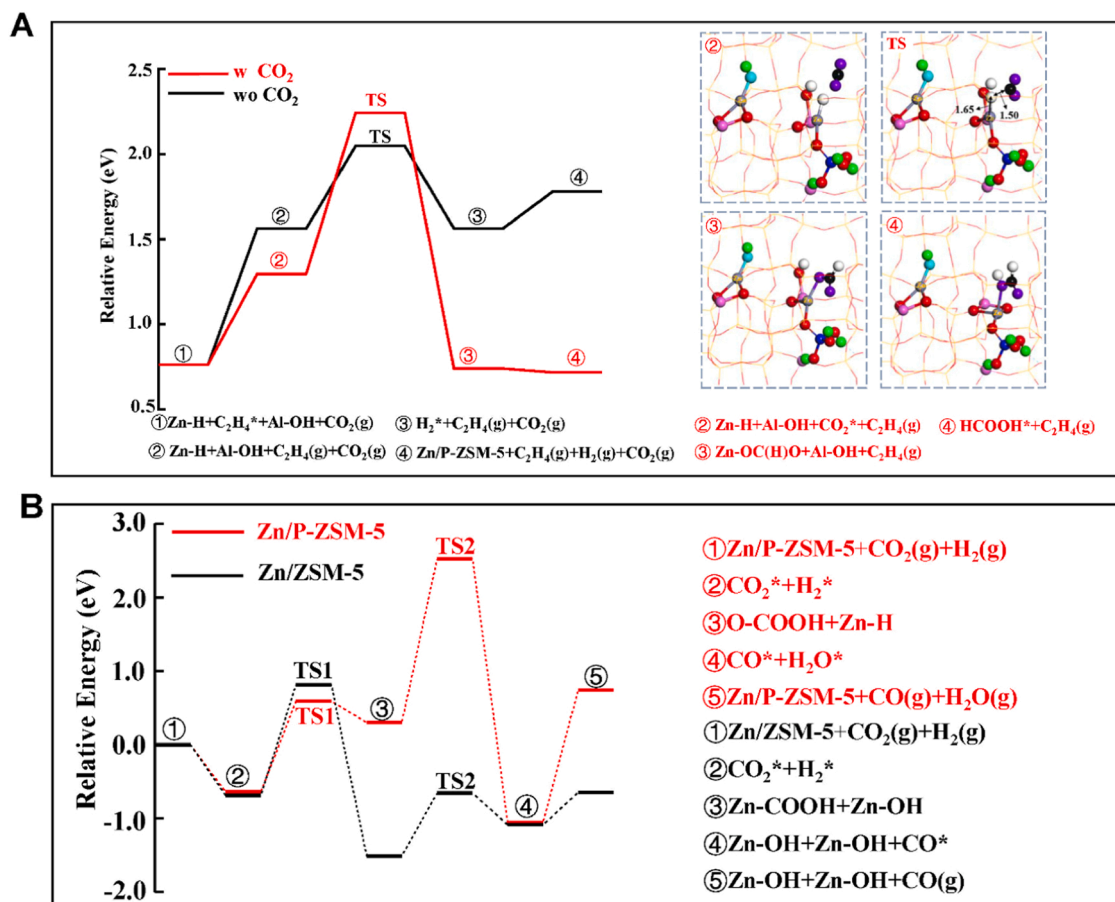

Fig. 7. Energy diagrams of (A) barrier calculations for H_2 formation step in ethane dehydrogenation to ethylene for the cases in the absence and presence of CO_2. (B) the reaction of CO_2 with H_2 to produce CO and H_2O via RWGS over Zn/ZSM-5 and Zn/P-ZSM-5.

toward both ethane and CO_2 than the other two sites, thus being the main active site for reactant adsorption and reaction. The most stable CO_2 adsorption configuration has an adsorption energy of -0.59 eV, equivalent to that of the energetically most favorable ethane adsorption. The similar adsorption energies suggest that CO_2 competes with ethane adsorption at the P-O-Zn active site, thus resulting in the decreased ethane conversion as observed experimentally (Fig. 3A).

On the other hand, the consumption of H_2 generated from the reaction of ethane aromatization via the RWGS reaction was examined on Zn/P-ZSM-5 and Zn/ZSM-5. The energetically favorable pathways were shown in Fig. 7B and relevant structures were provided in Fig. S15. Over Zn/P-ZSM-5, CO_2 and H_2 were more likely to react to form Zn-H and O-COOH, which had a barrier of 1.23 eV. Subsequently, the Zn-H and O-COOH reacted to produce CO and H_2O with a large barrier of 2.23 eV. Over Zn/ZSM-5, the high barrier step of CO_2 reacting with H_2 had a barrier of 1.50 eV, lower than that (2.23 eV) obtained over Zn/P-ZSM-5, indicating that the introduction of P hindered the RWGS reaction, thus suppressing the formation of H_2O. A previous work demonstrated a negative effect of H_2O on both the stability of Zn/ZSM-5 catalyst and ethane conversion [7], however, the CO_2-ODA over Zn/P-ZSM-5 was more stable in regard to ethane conversion and aromatics formation. Therefore, CO_2 tended to participate in the main reaction of ethane conversion to avoid the formation of H_2 molecule instead of going through the RWGS reaction over Zn/P-ZSM-5, which was able to suppress the Zn evaporation and enhance catalyst stability as observed in the results of ICP-AES.

4. Conclusions

In summary, we reported CO_2-assisted ethane aromatization under ambient pressure over P-modified Zn/ZSM-5 catalysts. *In situ* AP-XPS and XAFS characterization and DFT calculations were used to analyze the structural evolution of the catalysts. Mainly isolated Zn^{2+} species from the transformation of $[Zn(OH)]^+$ were found when the catalysts were exposed in the reaction conditions (CO_2 and ethane, 800 K). The evaporation of Zn species on the catalyst was significantly suppressed in the CO_2-ODA reaction via inhibiting the generation of molecular H_2. The incorporation of P significantly enhanced the aromatics selectivity of Zn/ZSM-5. The presence of CO_2 reduced the deactivation rate via promoting the consumption of deposited carbon and retarding the zinc loss, which could facilitate the generation of liquid aromatics accompanied with a simultaneous reduction of CO_2 to CO.

CRediT authorship contribution statement

C.T., **H.F.** and **D.W.** contributed equally to this work. **C.T.** and **J.G.C.** conceived the idea and designed the experiments. **C.T.** performed the catalyst preparation, characterizations, and data analysis. **C.T.** and **D.W.** conducted the catalytic performance tests. **Z.X.** and **Y.D.** carried out the *in situ* XAFS experiments and analyzed the XAFS data. **N.R.** and **S.D.S.** conducted the AP-XPS measurements. **H.F.** and **X.N.** performed the DFT calculations. **C.T.**, **H.F.**, **Z.X.**, **X.N.** and **J.G.C.** wrote the manuscript. **J.G.C.** reviewed and edited the manuscript, and supervised the whole project.

Declaration of Competing Interest

The authors declare that they have no known competing financial interests or personal relationships that could have appeared to influence the work reported in this paper.

Acknowledgements

Appendix A. Supporting information

Supplementary data associated with this article can be found in the online version at doi:10.1016/j.apcatb.2021.120956.

References

[1] E. Gomez, B. Yan, S. Kattel, J.G. Chen, Carbon dioxide reduction in tandem with light-alkane dehydrogenation, Nat. Rev. Chem. 3 (2019) 638–649.

[2] G. Li, C. Liu, X. Cui, Y. Yang, F. Shi, Oxidative dehydrogenation of light alkanes with carbon dioxide, Green Chem. 23 (2021) 689–707.

[3] B. Yan, S. Yao, S. Kattel, Q. Wu, Z. Xie, E. Gomez, P. Liu, D. Su, J.G. Chen, Active sites for tandem reactions of CO_2 reduction and ethane dehydrogenation, Proc. Natl. Acad. Sci. USA 115 (2018) 8278–8283.

[4] Z. Xie, D. Tian, M. Xie, S.-Z. Yang, Y. Xu, N. Rui, J.H. Lee, S.D. Senanayake, K. Li, H. Wang, S. Kattel, J.G. Chen, Interfacial active sites for CO_2 assisted selective cleavage of C–C/C–H bonds in ethane, Chem 6 (2020) 2703–2716.

[5] Z. Xie, L.R. Winter, J.G. Chen, Bimetallic-derived catalysts and their application in simultaneous upgrading of CO_2 and ethane, Matter 4 (2021) 408–440.

[6] Z. Xie, E. Gomez, J.G. Chen, Simultaneously upgrading CO_2 and light alkanes into value-added products, AIChE J. 67 (2021), e17249.

[7] H. Fan, X. Nie, H. Wang, M.J. Janik, C. Song, X. Guo, Mechanistic understanding of ethane dehydrogenation and aromatization over Zn/ZSM-5: effects of Zn modification and CO_2 co-reactant, Catal. Sci. Technol. 10 (2020) 8359–8373.

[8] A. Mehdad, R.F. Lobo, Ethane and ethylene aromatization on zinc-containing zeolites, Catal. Sci. Technol. 7 (2017) 3562–3572.

[9] J. Gao, C. Wei, M. Dong, G. Wang, Z. Li, Z. Qin, J. Wang, W. Fan, Evolution of Zn species on Zn/HZSM-5 catalyst under H_2 pretreated and its effect on ethylene aromatization, ChemCatChem 11 (2019) 3892–3902.

[10] A. Samanta, X. Bai, B. Robinson, H. Chen, J. Hu, Conversion of light alkane to value-added chemicals over ZSM-5/metal promoted catalysts, Ind. Eng. Chem. Res. 56 (2017) 11006–11012.

[11] Y. Cheng, T. Lei, C. Miao, W. Hua, Y. Yue, Z. Gao, Ga_2O_3/NaZSM-5 for C_2H_6 dehydrogenation in the presence of CO_2: Conjugated effect of silanol, Microporous Mesoporous Mater. 268 (2018) 235–242.

[12] E. Gomez, X. Nie, J.H. Lee, Z. Xie, J.G. Chen, Tandem reactions of CO_2 reduction and ethane aromatization, J. Am. Chem. Soc. 141 (2019) 17771–17782.

[13] J. Liu, N. He, W. Zhou, L. Lin, G. Liu, C. Liu, J. Wang, Q. Xin, G. Xiong, H. Guo, Isobutane aromatization over a complete Lewis acid Zn/HZSM-5 zeolite catalyst: performance and mechanism, Catal. Sci. Technol. 8 (2018) 4018–4029.

[14] A.G. Stepanov, M.V. Luzgin, V.N. Romannikov, V.N. Sidelnikov, E.A. Paukshtis, The nature, structure, and composition of adsorbed hydrocarbon products of ambient temperature oligomerization of ethylene on acidic zeolite H-ZSM-5, J. Catal. 178 (1998) 466–477.

[15] E.A. Uslamin, H. Saito, N. Kosinov, E. Pidko, Y. Sekine, E.J.M. Hensen, Aromatization of ethylene over zeolite-based catalysts, Catal. Sci. Technol. 10 (2020) 2774–2785.

[16] J. Liu, L. Lin, J. Wang, W. Zhou, C. Miao, C. Liu, N. He, Q. Xin, H. Guo, Transient Brønsted acid sites in propene aromatization over Zn-modified HZSM-5 detected by operando dual-beam FTIR, J. Phys. Chem. C 123 (2019) 7283–7289.

[17] H. Saito, Y. Sekine, Catalytic conversion of ethane to valuable products through non-oxidative dehydrogenation and dehydroaromatization, RSC Adv. 10 (2020) 21427–21453.

[18] J.A. Biscardi, G.D. Meitzner, E. Iglesia, Structure and density of active Zn species in Zn/H-ZSM5 propane aromatization catalysts, J. Catal. 179 (1998) 192–202.

[19] Y. Zhang, S. Wu, X. Xu, H. Jiang, Ethane aromatization and evolution of carbon deposits over nanosized and microsized Zn/ZSM-5 catalysts, Catal. Sci. Technol. 10 (2020) 835–843.

[20] G. Kresse, J. Furthmüller, Efficiency of ab-initio total energy calculations for metals and semiconductors using a plane-wave basis set, Comput. Mater. Sci. 6 (1996) 15–50.

[21] G. Kresse, D. Joubert, From ultrasoft pseudopotentials to the projector augmented-wave method, Phys. Rev. B 59 (1999) 1758–1775.

[22] P.E. Blöchl, Projector augmented-wave method, Phys. Rev. B 50 (1994) 17953–17979.

[23] J.P. Perdew, K. Burke, M. Ernzerhof, Generalized gradient approximation made simple, Phys. Rev. Lett. 77 (1996) 3865–3868.

[24] S. Grimme, J. Antony, T. Schwabe, C. Mück-Lichtenfeld, Density functional theory with dispersion corrections for supramolecular structures, aggregates, and complexes of (bio)organic molecules, Org. Biomol. Chem. 5 (2007) 741–758.

[25] S. Grimme, Accurate description of van der Waals complexes by density functional theory including empirical corrections, J. Comput. Chem. 25 (2004) 1463–1473.

[26] G. Henkelman, B.P. Uberuaga, H. Jónsson, A climbing image nudged elastic band method for finding saddle points and minimum energy paths, J. Chem. Phys. 113 (2000) 9901–9904.

[27] E.A. Pidko, R.A. van Santen, Activation of light alkanes over zinc species stabilized in ZSM-5 zeolite: a comprehensive DFT study, J. Phys. Chem. C 111 (2007) 2643–2655.

[28] Y. Chu, X. Gao, X. Zhang, G. Xu, G. Li, A. Zheng, Identifying the effective phosphorous species over modified P-ZSM-5 zeolite: a theoretical study, Phys. Chem. Chem. Phys. 20 (2018) 11702–11712.

[29] K. Damodaran, J.W. Wiench, S.M. Cabral de Menezes, Y.L. Lam, J. Trebosc, J. P. Amoureux, M. Pruski, Modification of H-ZSM-5 zeolites with phosphorus. 2. Interaction between phosphorus and aluminum studied by solid-state NMR spectroscopy, Microporous Mesoporous Mater. 95 (2006) 296–305.

[30] J. Caro, M. Bülow, M. Derewinski, J. Haber, M. Hunger, J. Kärger, H. Pfeifer, W. Storek, B. Zibrowius, NMR and IR studies of zeolite H-ZSM-5 modified with orthophosphoric acid, J. Catal. 124 (1990) 367–375.

[31] T. Blasco, A. Corma, J. Martínez-Triguero, Hydrothermal stabilization of ZSM-5 catalytic-cracking additives by phosphorus addition, J. Catal. 237 (2006) 267–277.

[32] J. Zhuang, D. Ma, G. Yang, Z. Yan, X. Liu, X. Liu, X. Han, X. Bao, P. Xie, Z. Liu, Solid-state MAS NMR studies on the hydrothermal stability of the zeolite catalysts for residual oil selective catalytic cracking, J. Catal. 228 (2004) 234–242.

[33] H.E. Mason, S. Frisia, Y. Tang, R.J. Reeder, B.L. Phillips, Phosphorus speciation in calcite speleothems determined from solid-state NMR spectroscopy, Earth Planet. Sci. Lett. 254 (2007) 313–322.

[34] G. Qi, Q. Wang, J. Xu, J. Trébosc, O. Lafon, C. Wang, J.-P. Amoureux, F. Deng, Synergic effect of active sites in zinc-modified ZSM-5 zeolites as revealed by high-field solid-state NMR spectroscopy, Angew. Chem. Int. Ed. 55 (2016) 15826–15830.

[35] J.-F. Wu, S.-M. Yu, W.D. Wang, Y.-X. Fan, S. Bai, C.-W. Zhang, Q. Gao, J. Huang, W. Wang, Mechanistic insight into the formation of acetic acid from the direct conversion of methane and carbon dioxide on zinc-Modified H–ZSM-5 zeolite, J. Am. Chem. Soc. 135 (2013) 13567–13573.

[36] H.E. van der Bij, B.M. Weckhuysen, Phosphorus promotion and poisoning in zeolite-based materials: synthesis, characterisation and catalysis, Chem. Soc. Rev. 44 (2015) 7406–7428.

[37] J. Zhang, X. Zhu, S. Zhang, M. Cheng, M. Yu, G. Wang, C. Li, Selective production of para-xylene and light olefins from methanol over the mesostructured Zn–Mg–P/ZSM-5 catalyst, Catal. Sci. Technol. 9 (2019) 316–326.

[38] P. Li, W. Zhang, X. Han, X. Bao, Conversion of methanol to hydrocarbons over phosphorus-modified ZSM-5/ZSM-11 intergrowth zeolites, Catal. Lett. 134 (2010) 124–130.

[39] X. Wang, W. Dai, G. Wu, L. Li, N. Guan, M. Hunger, Phosphorus modified HMCM-22: Characterization and catalytic application in methanol-to-hydrocarbons conversion, Microporous Mesoporous Mater. 151 (2012) 99–106.

[40] J. Nunan, J. Cronin, J. Cunningham, Combined catalytic and infrared study of the modification of H-ZSM-5 with selected poisons to give high p-xylene selectivity, J. Catal. 87 (1984) 77–85.

[41] J.G. Chen, NEXAFS investigations of transition metal oxides, nitrides, carbides, sulfides and other interstitial compounds, Surf. Sci. Rep. 30 (1997) 1–152.

[42] N.Z. Logar, N.N. Tušar, A. Ristić, G. Mali, M. Mazaj, V. Kaučič, Chapter 5 - Functionalisation and structure characterisation of porous silicates and aluminophosphates, in: V. Valtchev, S. Mintova, M. Tsapatsis (Eds.), Ordered Porous Solids, Elsevier, Amsterdam, 2009, pp. 101–126.

[43] M.H. Mahyuddin, S. Tanaka, Y. Shiota, K. Yoshizawa, Room-temperature activation of methane and direct formations of acetic acid and methanol on Zn-ZSM-5 zeolite: a mechanistic DFT study, Bull. Chem. Soc. Jpn. 93 (2020) 345–354.

[44] J.S. Jarvis, J.H. Harrhy, P. He, A. Wang, L. Liu, H. Song, Highly selective aromatization and isomerization of n-alkanes from bimetallic Pt–Zn nanoparticles supported on a uniform aluminosilicate, Chem. Commun. 55 (2019) 3355–3358.

[45] Q. Che, M. Yang, X. Wang, Q. Yang, L. Rose Williams, H. Yang, J. Zou, K. Zeng, Y. Zhu, Y. Chen, H. Chen, Influence of physicochemical properties of metal modified ZSM-5 catalyst on benzene, toluene and xylene production from biomass catalytic pyrolysis, Bioresour. Technol. 278 (2019) 248–254.

[46] A.A. Gabrienko, S.S. Arzumanov, A.V. Toktarev, I.G. Danilova, I.P. Prosvirin, V. V. Kriventsov, V.I. Zaikovskii, D. Freude, A.G. Stepanov, Different efficiency of Zn^{2+} and ZnO species for methane activation on Zn-modified zeolite, ACS Catal. 7 (2017) 1818–1830.

[47] I. Pinilla-Herrero, E. Borfecchia, J. Holzinger, U.V. Mentzel, F. Joensen, K. A. Lomachenko, S. Bordiga, C. Lamberti, G. Berlier, U. Olsbye, S. Svelle, J. Skibsted, P. Beato, High Zn/Al ratios enhance dehydrogenation vs hydrogen transfer reactions of Zn-ZSM-5 catalytic systems in methanol conversion to aromatics, J. Catal. 362 (2018) 146–163.

[48] S.M.T. Almutairi, B. Mezari, P.C.M.M. Magusin, E.A. Pidko, E.J.M. Hensen, Structure and reactivity of Zn-modified ZSM-5 zeolites: the importance of clustered cationic Zn complexes, ACS Catal. 2 (2012) 71–83.

[49] C. Hennig, K.-H. Hallmeier, G. Zahn, F. Tschwatschal, H. Hennig, Conformational influence of dithiocarbazinic acid bishydrazone ligands on the structure of zinc(II) complexes: a comparative XANES study, Inorg. Chem. 38 (1999) 38–43.

[50] V. Yachandra, L. Powers, T.G. Spiro, X-ray absorption spectra and the coordination number of zinc and cobalt carbonic anhydrase as a function of pH and inhibitor binding, J. Am. Chem. Soc. 105 (1983) 6596–6604.

[51] Y. Chen, K. Gong, F. Jiao, X. Pan, G. Hou, R. Si, X. Bao, C–C bond formation in syngas conversion over zinc sites grafted on ZSM-5 zeolite, Angew. Chem. Int. Ed. 59 (2020) 6529–6534.

[52] X. Niu, X. Nie, C. Yang, J.G. Chen, CO_2-Assisted propane aromatization over phosphorus-modified Ga/ZSM-5 catalysts, Catal. Sci. Technol. 10 (2020) 1881–1888.

[53] J. Liu, N. He, Z. Zhang, J. Yang, X. Jiang, Z. Zhang, J. Su, M. Shu, R. Si, G. Xiong, H.-b. Xie, G. Vilé, Highly-dispersed zinc species on zeolites for the continuous and selective dehydrogenation of ethane with CO_2 as a soft oxidant, ACS Catal. 11 (2021) 2819–2830.

[54] V. Abdelsayed, D. Shekhawat, M.W. Smith, Effect of Fe and Zn promoters on Mo/HZSM-5 catalyst for methane dehydroaromatization, Fuel 139 (2015) 401–410.